nature communications

Article

https://doi.org/10.1038/s41467-026-68756-y

Breaking activity-selectivity-stability trade-offs in reverse water-gas shift reaction via high-energy micro-faceted Mo_2N nanocrystals

Received: 25 June 2025

Accepted: 15 January 2026

Published online: 02 February 2026

Check for updates

Jinshu Tian[1,4], Ling Fang[1,4], Ni Ouyang[1,4], Liwei Xia[1,4], Zhi Wang[1], Haiting Cai[1] ✉, Qilong Feng[1], Xinru Jiang[1], Jia Zhao[1], Mingwu Tan[2], Lili Zhang[2], Yong Wang[3] ✉, Xiaonian Li[1] ✉ & Yihan Zhu[1] ✉

The reverse water-gas shift reaction (RWGSR) is essential for converting CO_2 into fuels using renewable hydrogen, but it remains challenged by the difficulty of simultaneously maximizing catalyst activity, selectivity, and stability. These limitations stem from thermodynamic constraints – specifically, the Gibbs-Curie-Wulff theorem - which restricts the synthetic accessibility of high-energy micro-faceted nanocrystals via conventional methods. To address this, we introduce a near-surface "quasi-hyperbaric" ammonia strategy that integrates atmospheric-pressure processing with in-situ ammonia decomposition. This approach enables the controlled synthesis of molybdenum nitride nanocrystals with preferentially exposed high-energy (112) microfacets. These facets promote CO_2 activation through a hydrogen-assisted redox mechanism, driven by geometrically confined and stabilized Mo-N/M-O hybrid active sites. The resulting catalyst outperforms the benchmark Pt/CeO_2, which typically suffers from CO selectivity below 92%. Our catalyst achieves near-equilibrium conversion (56%) at a space velocity (24000 $ml/g_{cat}/h$), with 100% CO selectivity and outstanding stability (≤ 1% deactivation over 250 hours).

Catalytic conversion of CO_2 to CO via the reverse water-gas shift reaction (RWGSR) is a key pathway for sustainable fuel production and advancing carbon neutrality[1–3]. Despite its thermodynamic favorability at elevated temperatures, practical implementation of RWGSR is limited by the lack of catalysts that concurrently offer near-equilibrium conversion, perfect selectivity and industrial-grade stability[4–6]. This performance paradox arises from intrinsic trade-offs between the reactivity of catalytically active sites and their thermodynamic stability during synthesis and reaction. Although high-energy active sites, such as the high-energy microfacets of nanocrystals, are expected to enhance CO production[7], the creation of these metastable states poses significant challenges. Unfortunately, they also accelerate catalyst sintering and side reactions, which compromise selectivity and stability.

Conventional catalyst systems exemplify this dilemma. While Pt-group catalysts are active and robust, they suffer from CO selectivity

[1]Center for Electron Microscopy, Zhejiang Key Laboratory of Surface and Interface Science and Engineering for Catalysts, China-Saudi Arabia Joint Laboratory on Microscopic Structural Engineering of Advanced Materials, State Key Laboratory of Green Chemical Synthesis and Conversion and College of Chemical Engineering, Zhejiang University of Technology, Hangzhou, P. R. China. [2]Institute of Sustainability for Chemicals, Energy and Environment, Agency for Science, Technology and Research, 1 Pesek Road, Jurong, Island, Singapore. [3]Voiland School of Chemical Engineering and Bioengineering, Washington State University, Pullman, WA, USA. [4]These authors contributed equally: Jinshu Tian, Ling Fang, Ni Ouyang, Liwei Xia. ✉e-mail: haiting.cai@pnnl.gov; wang42@wsu.edu; xnli@zjut.edu.cn; yihanzhu@zjut.edu.cn

loss above 400 °C due to unfavorable electronic state transitions under reducing conditions[8–10]. Conversely, Cu-based catalysts offer high selectivity but lack sufficient activity and thermal instability, limited by their low Tamman temperature and a tendency for excessive hydrogenation[3,11,12]. Emerging transition metal nitrides and carbides, particularly molybdenum nitride (Mo_2N) nanocrystals, show promise in bridging this gap by mimicking noble metal behavior while offering superior thermal stability[1,5,13–18]. However, conventional synthesis routes for Mo_2N nanocrystals constrained by Gibbs-Curie-Wulff thermodynamic principles, inevitably expose low-energy microfacets as global surface energy minima through the predictive Wulff reconstruction, compromising the activity towards the RWGSR reaction[19,20]. To address the thermodynamic constraint, it is crucial to implement a kinetic control strategy that stabilizes highly active metastable microfacets by overriding the surface termination configurations at global energy minima. A viable approach involves introducing an intermediate stage characterized by a non-equilibrium steady-state chemical environment, guiding unconventional crystal growth during chemical synthesis. This strategy facilitates the formation of high-energy metastable microfacets in nanocrystals under synthetic conditions, allowing them to be effectively maintained and stabilized upon quenching.

As a proof-of-concept study, we introduce a near-surface "quasi-hyperbaric" ammonia atmosphere as a non-equilibrium steady-state chemical environment that completely alters the growth kinetics of Mo_2N nanocrystals restricted by the Gibbs-Curie-Wulff theorem. This is achieved by imposing strong surface-adsorbate interaction onto the intermediate structures during crystal growth, which completely alters the micro-faceting behaviors of nanocrystals and leads to the formation of high-energy (112) microfacets instead of thermodynamically stable (001)/(111) microfacets as predicted by Wulff construction. The high-energy-micro-faceted molybdenum nitride nanocrystal (HEMN) performs as a catalyst and demonstrates exceptional CO_2 hydrogenation performance, achieving 56% near-equilibrium CO_2 conversion with 100% CO selectivity at 550 °C and a space velocity of 24,000 $mL{\cdot}g^{-1}{\cdot}h^{-1}$, while maintaining excellent stability (< 1% activity loss over 250 + hours). Notably, HEMN outperforms noble-metal benchmarks, sustaining 100% CO selectivity compared to < 92% for Pt-based catalysts under equivalent conditions. The in situ spectroscopy, reaction kinetic analysis, and DFT calculations reveal that Mo-N/M-O hybrid structures on (112) microfacets act as active sites for CO_2 activation via an H_2-assisted redox mechanism.

Results

The creation of HEMN catalysts

The growth of Mo_2N nanocrystals is influenced by the point symmetry of the tetragonal crystal lattice and thermodynamic constraints defined by the Gibbs-Curie-Wulff theorem. Consequently, conventional chemical synthesis typically results in Mo_2N nanocrystals featuring low-energy microfacets, as predicted by Wulff construction. This characteristic can be assessed through the surface free energy plot, or γ-plot, illustrated in Fig. 1a for the Mo_2N crystal structure projected along the (110) direction under vacuum conditions (red contour). Notably, the γ-plot under vacuum displays multiple cusped minima at 0.1003, 0.1121, 0.0977, and 0.1009 eV/Å² along the normals of the (001), (112), (111), and (110) microfacets. These cusped minima emerge from the lateral growth of Mo_2N nanocrystals, following the classical terrace-ledge-kink model. The surface energies of these microfacets are ranked as (111) < (001) < (110) < (112) (Fig. 1 and Supplementary Figs. S1, S2). The Wulff construction under vacuum would therefore lead to an enclosure of the low-energy (001) and (111) microfacets, resulting in Mo_2N nanocrystals shaped like truncated elongated octahedra. To overcome the thermodynamic restrictions associated with these stable microfacets, a near-surface "quasi-hyperbaric" ammonia atmosphere was introduced as a non-equilibrium steady-state, integrating both atmospheric and on-site decomposed ammonia (Supplementary Fig. S3a). This "quasi-hyperbaric" environment modulates the growth kinetics of Mo_2N nanocrystals by significantly enhancing the surface-adsorbate interaction. Investigating the γ-plot of Mo_2N surfaces bonded with ammonia adsorbates (purple contour) reveals that the interaction dramatically alters the surface energies of the nanocrystals. The chemical bonding of ammonia molecules decreases the surface energies for all microfacets at the cusped minima of the γ-plot, with a particularly pronounced effect on the (112) microfacets (approximately a 45% reduction in surface energy, from 0.1121 eV/Å² to 0.0648 eV/Å²). Consequently, the surface energies are re-ranked to (112) < (111) < (110) < (001), leading to the tentative stabilization of the high-energy (112) microfacets under synthetic conditions. Metastable nanocrystals in HEMN catalysts with exposed (112) microfacets and an octahedral shape can be synthesized by creating a near-surface "quasi-hyperbaric" ammonia atmosphere based on Wulff construction.

The experimental validation of HEMN catalysts can be achieved through combined high-resolution scanning transmission electron microscopy (HR-STEM) and electron tomography (ET). Multimodal STEM imaging, which incorporates high-angle annular dark-field (HAADF) and integrated differential phase contrast (iDPC) modes, enables the simultaneous visualization of both heavy and light elements within the Mo_2N nanocrystals. HAADF-STEM images captured along the [021] and [001] zone axes (Fig. 1d, h) clearly depict projected polyhedral nanocrystals measuring 5–10 nm (Supplementary Figs. S4, S5) with regular shapes. The angular gaps measured between the projected microfacets of these nanocrystals are 75° and 91°, respectively, aligning with the crystallographic interplanar angle for (112) microfacets. This observation supports the octahedral model predicted by Wulff construction (Fig. 1a). In addition, the explicit three-dimensional (3D) morphology of the nanocrystals can be reconstructed using the ET method based on tilt-series of STEM images, as illustrated in Fig. 1c and Supplementary Fig. S6. The Gaussian surface curvature of the 3D tomogram reveals that a randomly selected Mo_2N nanocrystal exhibits an octahedral shape, enclosed by microfacets shown in blue and connected by edges depicted in yellow. These microfacets can be indexed to the (112) group of crystal faces by comparing the projections of the reconstructed tomogram with the HAADF-STEM image along the [021] axis (Fig. 1b, c and Supplementary Fig. S5). Such observations confirm the (112) micro-faceted structure of HEMN catalysts stabilized under a "quasi-hyperbaric" ammonia atmosphere as a non-equilibrium steady-state. Furthermore, atomic-resolution structural elucidation of Mo_2N nanocrystals is facilitated through combined HAADF- and iDPC-STEM imaging, as demonstrated in Fig. 1d, h and Fig. 1e, i. An enlarged view of the HAADF-STEM image along the [021] axis reveals hexagonally arranged bright spots indicative of Mo atomic columns (Fig. 1f). The nitrogen atoms residing in the octahedral voids of the Mo sublattice can be visualized as atomic columns in the iDPC-STEM image (Fig. 1j). The phase contrast images align well with both the structural projections and the simulated projected potential of the Mo_2N crystal structure (Fig. 1g, k). In summary, these observations robustly corroborate the proposed concept, strategy, and structural model of HEMN catalysts.

Evaluation of the RWGSR Performance

Systematic optimization of calcination conditions, support materials, and loading levels identified 30 wt% Mo_2N on silica, formed via ammonia calcination, as the optimal catalyst, exhibiting outstanding RWGSR activity (Supplementary Figs. S7, S8). We further conducted a comprehensive comparative analysis of the synthesized HEMN catalyst against representative RWGSR catalysts from the literature, evaluating key metrics including reaction rate ($mol/g^{-1}{*}h^{-1}$), CO selectivity, CO_2/H_2 ratio, deactivation rate, and catalyst synthesis complexity

https://doi.org/10.1038/s41467-026-68756-y

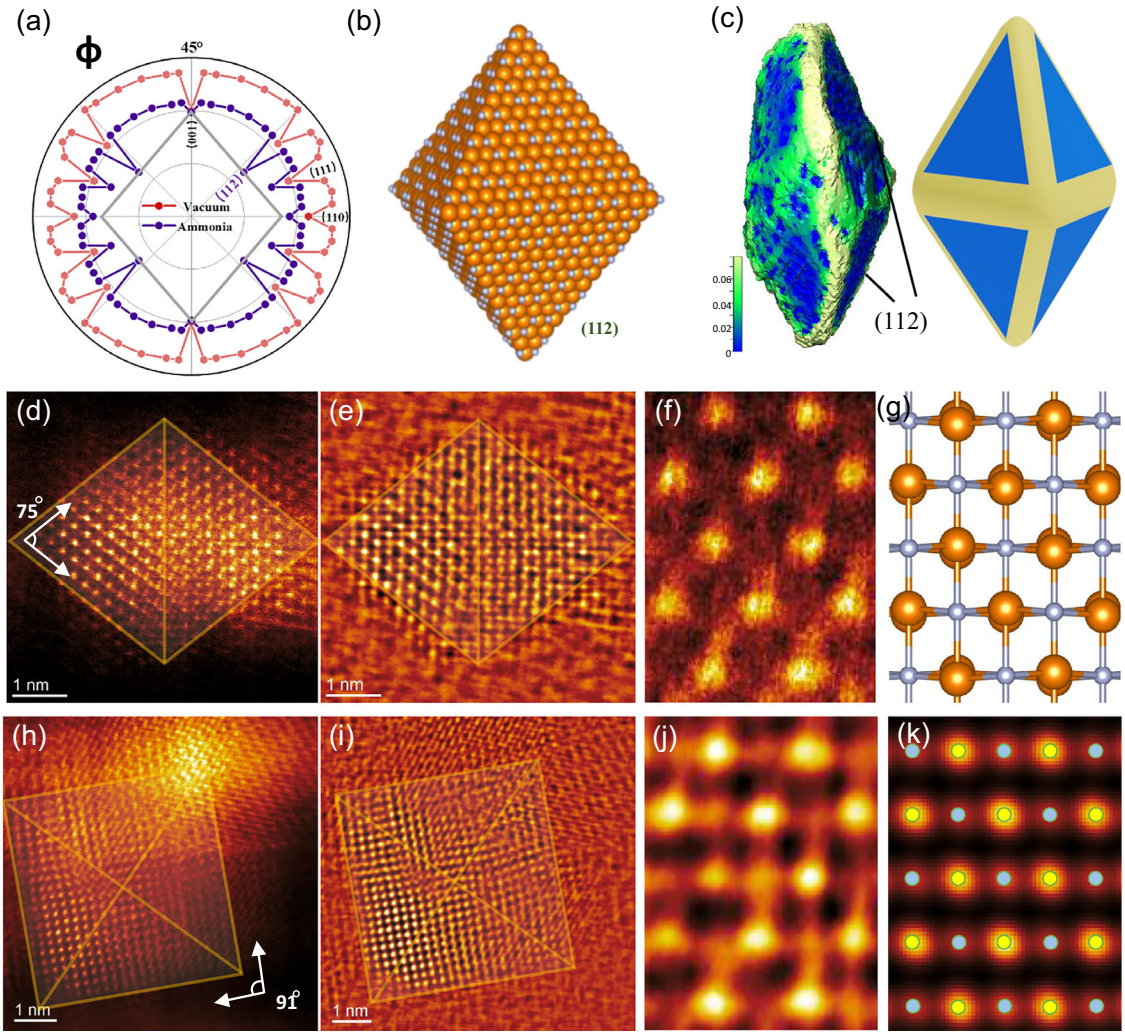

Fig. 1 | Structural elucidation of HEMN catalysts. a γ-plot under vacuum (red contour) and ammonia environmental conditions (purple contour), corresponding surface energy mapping. **b** 3D schematic of HEMN catalyst, with the terminating crystal facet as (112); **c** Electron tomography image of HEMN catalyst; Fine structure of HEMN catalyst along the [021] zone axis (**d**) HAADF-STEM and (**e**) iDPC-STEM imaging, as well as along the [001] zone axis (**h**) HAADF-STEM and (**i**) iDPC-STEM imaging, with orange lines indicating the particle shape in the projection direction; Magnified (**f**) HAADF-STEM image and (**j**) iDPC-STEM image along the [021] zone axis; (**g**) Structural model of HEMN and (**k**) corresponding simulated projected potential image (Mo atomic columns and N atomic columns are marked in yellow and blue solid circles, respectively).

(Supplementary Table S1). The HEMN catalyst demonstrated superior performance across all dimensions (Fig. 2a and Supplementary Fig. S10)[9,18,21,22]. Notably, within the high-temperature range (450–600 °C), the catalyst maintained nearly 100% CO selectivity across the full CO_2 conversion range (41.9%–62.6%). In contrast, Pt/CeO_2 exhibited a notable decrease in CO selectivity from 97.2% to 91.6% under the same reaction conditions (Fig. 2b and Supplementary Fig. S9). When evaluated under the same conditions, its overall performance exceeds that of other commonly reported catalysts (Supplementary Fig. S10). Additionally, the stoichiometric CO_2/H_2 ratio for the RWGSR is 1:1. However, in practical applications, a CO_2/H_2 ratio below 1:1 is often used to promote CO_2 reaction and generate syngas compatible with downstream conversion processes. Increasing the H_2 partial pressure thermodynamically favors the formation of methane formation[23]. To evaluate the effect of reactant composition, we investigated the influence of the CO_2/H_2 ratio on the catalytic performance. Increasing the H_2 partial pressure significantly enhanced CO_2 turnover rates while maintaining nearly 100% CO selectivity across both low (400 °C, in Supplementary Fig. S11) and high (550 °C, in Fig. 2c) temperature ranges. This behavior is a distinct feature of the Mo2N-based catalysts. Overall, the synthesized HEMN catalyst demonstrates robust performance over a broad temperature window (300–600 °C), wide space velocity range (12000 to 48000 ml/g_{cat}/h, shown in Supplementary Fig. S12), and varied CO_2/H_2 ratios (1:1 to 1:4).

Catalyst stability is a critical factor for its industrial application. To evaluate the stability of this HEMN catalyst in the RWGSR, we conducted long-term tests at both low (400 °C, in Supplementary Fig. S13) and high (550 °C, Fig. 2d) temperatures. For example, at 550 °C with a space velocity of 24000 ml/g_{cat}/h and a CO_2/H_2 ratio of 1/3, the catalyst exhibited only a slight decrease in conversion (from 52.6% to 52.1%) over 250 h, corresponding to just ~1% deactivation, which is significantly lower than values reported for similar catalytic systems[18]. Moreover, the catalyst demonstrated excellent cyclic stability under repeated temperature cycling between 300 °C and 550 °C (Fig. 2e). XRD analysis of the catalyst after thermal cycling revealed no significant changes in the catalyst's microstructure (Supplementary Fig. S14), further confirming its high-temperature stability. Moreover, the HEMN catalyst demonstrated exceptional high-temperature stability during a 12 h test at 600 °C, exhibiting no deactivation while maintaining consistent performance (Supplementary Fig. S15). Comprehensive characterization via in-situ and ex situ XRD (Supplementary Figs. S16, 17) and HRTEM (Supplementary Figs. S18, 19) confirmed

https://doi.org/10.1038/s41467-026-68756-y

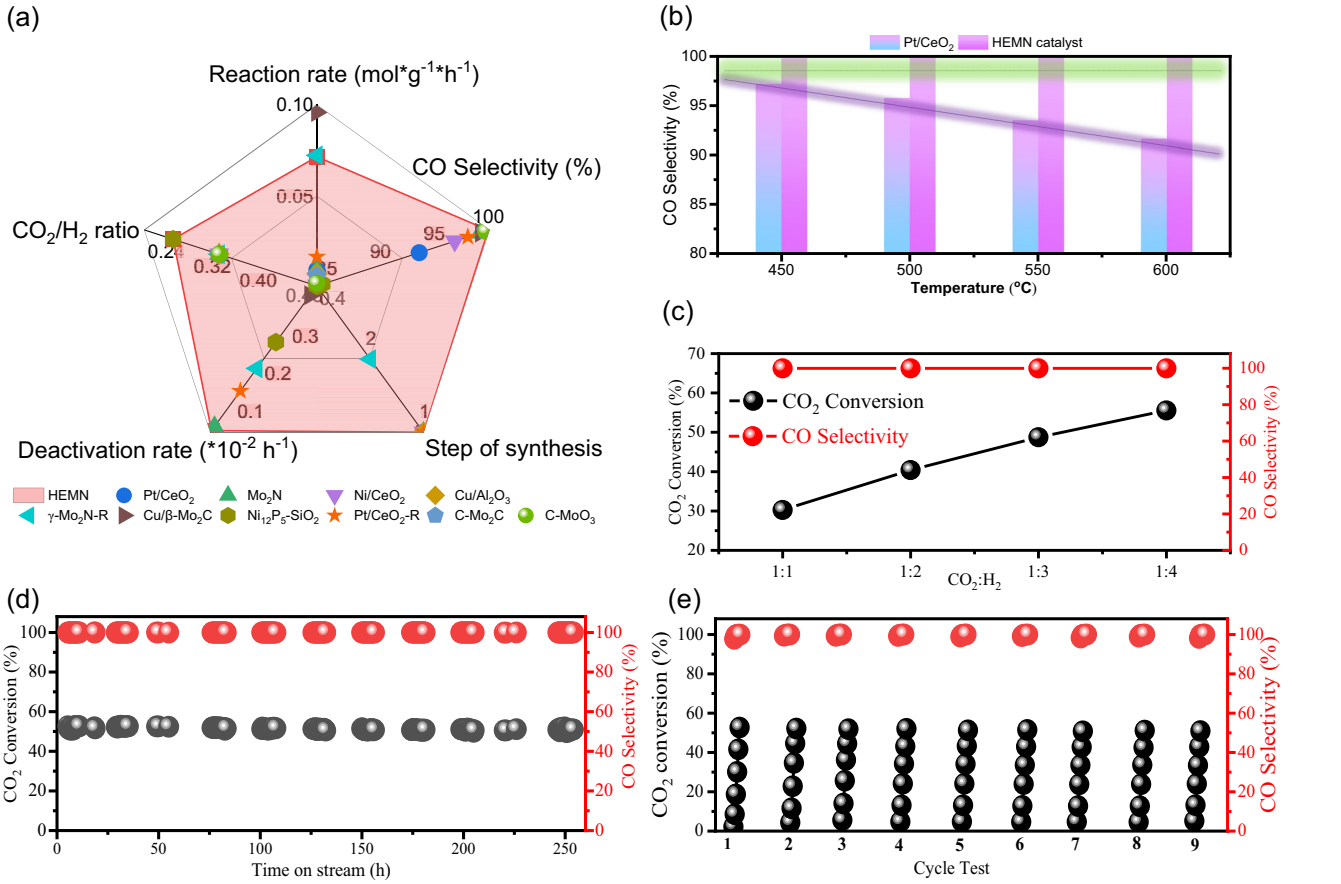

Fig. 2 | Catalytic performance of HEMN catalyst for RWGSR. a Radar chart shows comparing the synthesized HEMN catalyst with representative RWGSR catalysts reported in the references, where the number of synthesis steps is determined by the number of high-temperature calcination and post-treatment process (Supplementary Table S1 corresponds to the radar chart presented in Fig. 2a). **b** CO selectivity of the noble metal-based Pt/CeO_2 catalyst and the HEMN catalyst as a function of reaction temperature, under similar CO_2 conversion conditions, with a space velocity of 12600 ml/g_{cat}/h. **c** The effect of CO_2/H_2 ratio on CO_2 conversion and CO selectivity of this catalyst at 550 °C, with a space velocity of 18000 ml/g_{cat}/h. **d** Stability of this catalyst at 550 °C with a space velocity of 24000 mL/g_{cat}/h. **e** Cyclic stability test of this catalyst (repeated temperature cycling from 300 °C to 550 °C), conducted at a space velocity of 24000 mL/g_{cat}/h.

that both the phase structure and the specific (112) crystal facet remained stable without detectable thermodynamic reconstruction. These results collectively affirm the catalyst's robust performance and structural integrity under demanding operational conditions.

Active sites of the HEMN catalyst in the RWGSR

To elucidate the reasons for the high RWGSR activity of this HEMN catalyst, we performed surface structure analysis on the synthesized catalyst using XPS. As shown in Supplementary Fig. S20, the O 1*s* results revealed a peak at a binding energy of 530.6 eV, in addition to the characteristic peak of the support Si-O at 532.9 eV, which can be attributed to Mo-O species on the catalyst surface[24]. The Mo 3*d* results showed peaks at 228.9 eV and 231.8 eV, which can be attributed to Mo-N species, and peaks at 229.9 eV, 232.7 eV, and 232.5 eV, 235.2 eV, which correspond to two oxidation states of Mo-O species, Mo(IV) and Mo(VI)[25]. This further confirms the presence of a certain amounts of Mo-O species on the surface of this catalyst. To further investigate the redox properties of M-O species, we performed H_2-TPR-MS tests on the HEMN catalyst (Supplementary Figs. S21, S22). The results showed that compared to pure-phase MoO_3 (with a reduction onset temperature of ~ 600 °C), the Mo-O species on the HEMN catalyst surface are more easily reduced (with a reduction onset temperature of ~ 350 °C). This indicates that the Mo-O species on this HEMN catalyst are highly dispersed, consistent with the previously discussed HAADF-STEM structure (Supplementary Figs. S4, S5). These species have more active oxygen species, which can easily form a rich oxygen vacancy structure with high electron-donating capacity, acting as a scissor to directly cleave the C = O double bond of CO_2 to form CO[26].

To further explore the impact of Mo-O content on the catalytic performance of the RWGSR, we reduced the HEMN catalyst at different temperatures to construct a series of catalysts with varying Mo-O contents without destroying the Mo_2N crystalline phase structure (Supplementary Figs. S23 and S24). Supplementary Fig. S25 indicates that as the reduction temperature increases, the catalytic performance of the RWGSR gradually increases, reaching an optimal level when reduced at approximately 500 °C. When the reduction temperature is further increased, the CO_2 conversion decreases significantly (from 21.5% to 14.5%). Supplementary Fig. S26 shows a volcano-like relationship between Mo-O content and CO yield, indicating that the catalytic activity is optimal only when the Mo-O content (~ 4%, as determined by quantitative XPS analysis) on this catalyst surface is moderate. The activation of the C − O bond is crucial in the CO_2 hydrogenation reaction[27], and oxygen vacancies play a critical role[28]. At low reduction temperatures, the surface Mo-O concentration is high, resulting in weak CO_2 adsorption and hindered C-O bond cleavage, which collectively lead to reduced catalytic activity. At higher reduction temperatures, the surface Mo-O concentration decreases, exposing more oxygen vacancies and enhancing CO_2 adsorption. However, this also causes stronger adsorption of intermediate species, which hinders subsequent reactions[29] and reduces the overall reaction

https://doi.org/10.1038/s41467-026-68756-y

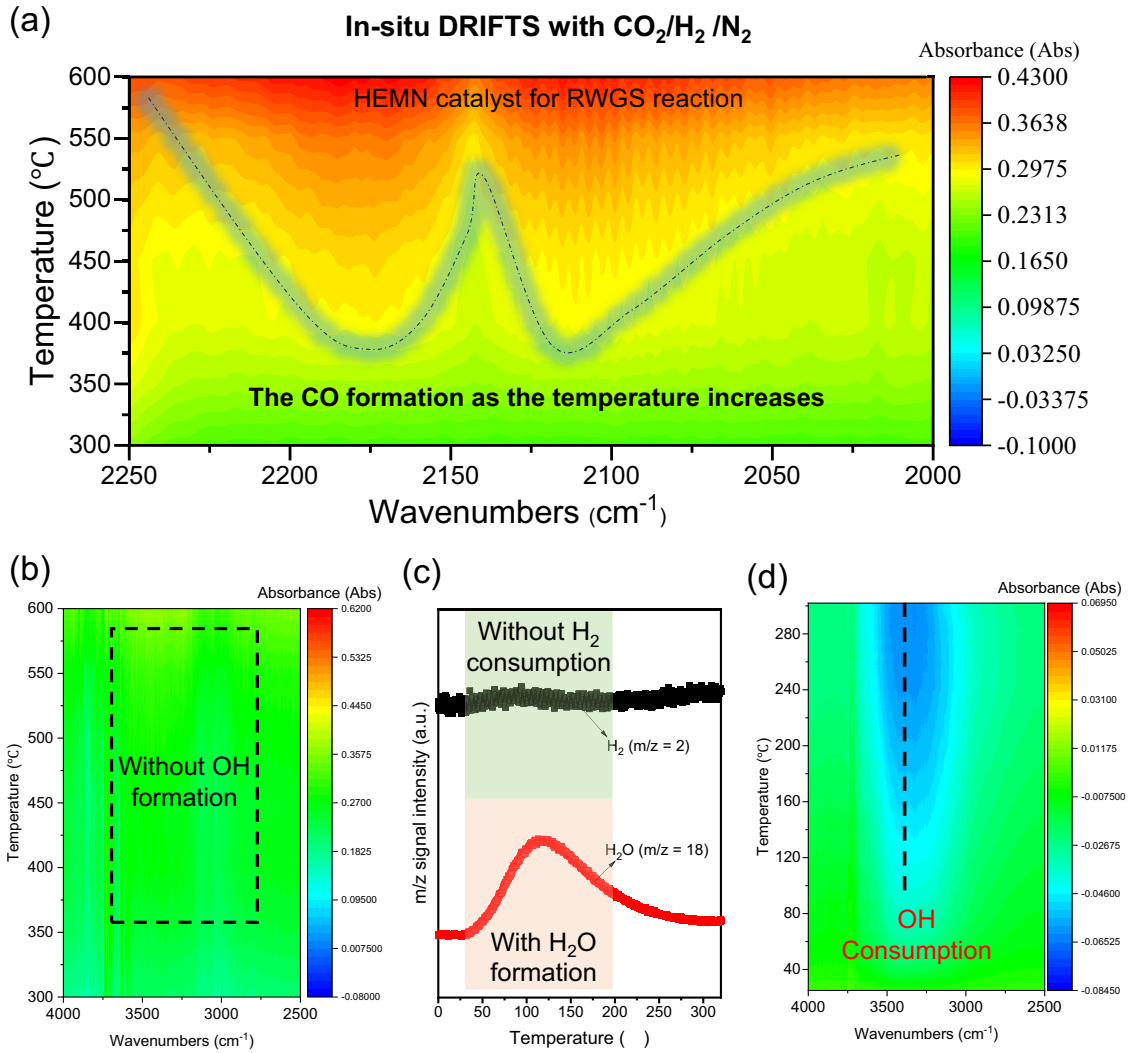

Fig. 3 | Study of the reaction pathway of the RWGSR over the HEMN catalyst. In situ DRIFTS at different temperatures: (**a**) 2250 cm^{-1} to 2000 cm^{-1}, (**b**) 4000 cm^{-1} to 2500 cm^{-1}; (**c**) H_2-TPR-MS profile of HEMN catalyst. **d** In situ DRIFTS of the HEMN catalyst in H_2/Ar atmosphere at different temperatures. Reaction conditions for catalysis: Catalyst mass: 12 mg, Gas composition: $CO_2/H_2/N_2$ = 24/72/4.

rate (Supplementary Fig. S27). Therefore, the Mo-O/Mo-N species on the surface of the HEMN catalyst are the key determinants of its catalytic activity, a conclusion supported by studies of other similar systems[30,31]

Reaction mechanism of the catalytic reaction

Depending on the interaction between CO_2 and H_2, the RWGSR can proceed via different mechanisms, including: the redox mechanism (where H* does not assist in C-O bond cleavage), the HCOO* pathway (H* directly hydrogenates C*), and the COOH* mechanism (H* directly hydrogenates O*)[5]. To investigate the reaction mechanism of the RWGSR on the HEMN catalyst, we tracked the intermediate species on the catalyst surface during the reaction using in situ IR experiments, as shown in Fig. 3a. The results showed that when the reaction gas ($CO_2/H_2/N_2$ = 24/72/4) was introduced, signals at 2175 cm^{-1} and 2120 cm^{-1} gradually appeared as the reaction temperature increased. These characteristic peaks can be attributed to the asymmetric and symmetric stretching vibrations of CO, respectively, as shown in Fig. 3a. Throughout the temperature ramping process (300 °C–600 °C), we did not observe the formation of any species related to COOH* or HCOO* (Supplementary Fig. S28), indicating that the hydrogenation of CO_2 on the HEMN catalyst does not follow the formate or carboxylate pathways. We hypothesize that the HEMN catalyst operates via the redox mechanism, in which CO_2 adsorbs on active sites, such as oxygen vacancies, followed by C-O bond cleavage to form CO and O species. To test this hypothesis, we introduced a CO_2/N_2 (30/70) mixture over the HEMN catalyst. If the redox mechanism were operative, CO* intermediates should be observed. However, unexpectedly, no CO* signals were detected under any of the following conditions: i) gradual temperature increase under CO_2/N_2 (Supplementary Fig. S29a), ii) The experiments involved either temperature ramping in 5% H_2/Ar after CO_2 adsorption at room temperature, or H_2 pre-adsorption followed by CO_2/N_2 exposure at varying temperatures (Supplementary Fig. S29b and **c**), or iii) after high temperatures reduction at 600 °C followed by similar in-situ experiments (Supplementary Figs. S30, S31). In addition, we complemented these studies with temperature-programmed surface reaction (TPSR) experiments and in-situ Raman measurements under CO_2/Ar atmosphere on the HEMN catalyst (Supplementary Fig. S32). Collectively, these results from both gas-phase and surface-sensitive characterization techniques consistently demonstrate that the reaction does not proceed via a conventional redox pathway, indicating a distinct mechanism deviating from the simple redox route.

Based on in situ experiments under reactive conditions (Fig. 3a), we conclude that CO* formation requires the presence of H_2, indicating a likely H_2-assisted redox mechanism, which is consistent with previous reports on the Mo_2C system[5]. Furthermore, throughout the reaction process (Fig. 3b and Supplementary Fig. S33), we observed no peaks forming or consuming in the range of 3500 cm^{-1} to 3200 cm^{-1}, which is attributed to the stretching vibrations of hydroxyl groups[32]. This indicates that the consumption or generation of OH/H_2O is a fast step in the elementary reactions and occurs after the rate-determining step[33].

During the H_2-TPR-MS test of the HEMN catalysts, we observed a significant formation of the H_2O peak before 300 °C (Fig. 3c). Since the samples were pre-treated in an inert atmosphere at 300 °C before the experiment, the adsorbed water on the samples was eliminated, ruling out the possibility that the H_2O peak was from desorption of adsorbed water. Simultaneous online mass spectrometry detection revealed no signal peaks at m/z = 2 (H_2 species), indicating that the H_2O peak did not originate from the reduction of surface metal oxide species. Infrared transmission spectroscopy of the HEMN catalyst revealed distinct surface Mo-OH species (Supplementary Fig. S34), suggesting that the H_2O peak detected by mass spectrometry likely originates from hydrogen-assisted dehydration of surface OH groups on the support.

To further verify this hypothesis, we conducted in situ IR experiments on the catalyst with H_2/Ar (Fig. 3d). The results showed a significant consumption of OH in a temperature range similar to that observed in the H_2-TPR-MS experiment, which is consistent with our hypothesis. When the HEMN samples were pretreated with hydrogen reduction at temperatures above 300 °C, there was no consumption of hydrogen observed in the in situ IR spectra. This finding confirms that surface Mo-OH species undergo hydrogen-assisted dehydration, forming Mo-O/Mo-N sites that constitute the active site structure, further supporting our earlier conclusions (Figs. S24–S27). Theoretical calculations further support this finding (Supplementary Figs.S35, S36), showing that the presence of H_2 lowers the dehydration energy of Mo-OH from 0.76/0.74 eV to 0.45/0.46 eV on Mo_2N (111) or (112) facets.

To further investigate the reaction mechanism of the RWGSR on the HEMN catalyst, we studied the kinetic dependences of CO_2 and H_2 at 300 °C and atmosphere pressure with 50.7–76.0 kPa H_2, and 10.1-35.5 kPa CO_2, when maintaining the CO_2 conversion below 10% and approach-to-equilibrium less than 10%. As shown in Fig. 4a, b, the turnover rate on HEMN catalyst gradually increased with the increasing partial pressure of CO_2, demonstrating a reaction order of 0.37 (± 0.003). The effect of H_2 partial pressure on the reaction rate showed a similar trend, with a reaction order of 0.28 (± 0.01). Combining the results from H_2-TPR-MS, CO-TPD, and in-situ IR spectroscopy experiments, we proposed the elementary reaction steps of the RWGSR on the HEMN catalyst, as shown in Fig. 4c. The reaction begins with the adsorption of CO_2 onto the Mo-O/N-Mo active site pair (denoted as *), forming adsorbed CO_2* (**Step 1**). Concurrently, H_2 undergoes dissociative adsorption at an adjacent site, producing an H* adatom and a Mo-OH* (**Step 2**). Subsequently, the H* species performs a nucleophilic attack on the oxygen atom of a nearby CO_2* molecule, cleaving the C = O bond to generate OH* and CO* intermediates (**Step 3**). The CO* intermediate then desorbs into the gas phase as CO (**Step 4**). Finally, two OH* species combine to form an H_2O* intermediate, which subsequently desorbs as a water molecule (**Steps 5 and 6**). Based on the above findings, together with the assumption of **Step 3** as the rate-determining step and the application of the pseudo steady-state approximation, we can obtain the following turnover rate equation, with the detailed derivation process given in the Supporting Information:

$$r = \frac{k\,K_{CO_2}(K_{H_2})^{0.5}[CO_2][H_2]^{0.5}}{\left(1+K_{CO_2}[CO_2]+\sqrt{K_{H_2}[H_2]}\right)^2} \quad (1)$$

where k and K_j (subscript $j = CO_2$ or H_2;) denote the rate constant of the kinetically relevant step (**Step 3**) and the equilibrium constant of the relevant elementary step (**Step 1** or **2**), respectively. The non-linear fitting of the experimental data with the turnover rate Eq. (1) determined $kK_{CO_2}(K_{H_2})^{0.5}$, K_{CO_2}, and K_{H_2} to be 3.32 (± 0.30) × 10^{-4} mol h^{-1} g_{cat}^{-1} $kPa^{-1.5}$, 0.041 (± 0.002) kPa^{-1}, and 5.01 (± 1.26) × 10^{-3} kPa^{-1}, respectively, as present in Fig. 4d. The predicted turnover rates closely match the experimental results, as confirmed by the parity plot (Fig. 4e). Under the operating conditions (50.7–76.0 kPa H_2, and 10.1-35.5 kPa CO_2), the coverage of unoccupied active site pairs on the catalyst surface varies from 33.3% to 52.1%, that of CO_2* from 20.4% to 49.2%, and that of H* from 17.0% to 30.4%. We also investigated catalytic systems with lower M-O content on HEMN reduced at 600°C, as shown in Supplementary Fig. S37, S38. The results indicate that the different M-O contents do not affect the reaction kinetics, such as the reaction orders and the rate-determining step.

To gain deeper mechanistic insights into the RWGSR catalyzed by the HEMN system, we conducted comprehensive theoretical investigations of the hydrogen-assisted CO_2 activation pathway, as illustrated in Fig. 5. Advanced electron microscopy coupled with 3D structural reconstruction unambiguously identified the preferential exposure of the (112) crystallographic facet in the HEMN catalyst, overriding the conventional thermodynamic stability of the (111) surface. Building on these experimental insights, we constructed DFT-optimized models of the dominant (112) and reference (111) surfaces of Mo_2N (Supplementary Fig. S39). To this end, we systematically probed the influence of Mo–O/N vacancy concentration on the H_2 binding energy, thereby identifying the Mo–O···H–Mo configuration as the initial active site for CO_2 activation (Supplementary Fig. S40). Comparative analysis of surface reactivity (Fig. 5 and Supplementary Fig. S41) revealed a striking reduction in the CO_2 dissociation energy barrier on the (112) surface (0.66 eV vs 1.14 eV on (111) facet), providing fundamental rationale for the exceptional catalytic performance of our engineered material compared to conventional Mo_2N systems.

To corroborate the hydrogen-mediated activation mechanism suggested by kinetic investigation and operando spectroscopic characterization, we systematically probed the hydrogen participation in CO_2 activation thermodynamics. DFT calculations demonstrate that on the (112) facet, the spontaneous conversion of adsorbed CO_2* to CO* and O* proceeds with an energy change of −1.20 eV under hydrogen-free conditions. Remarkably, the co-adsorption of H* species amplifies the thermodynamic favorability, lowering the energy change to −1.45 eV. Crucially, kinetic analyses revealed that hydrogen participation reduces the activation barrier from 0.66 eV to 0.45 eV, decisively confirming the viability of the H*-assisted activation pathway. In summary, our calculations demonstrate that the (112) facet is more active than the (111) facet for C–O bond cleavage, and that the H_2-assisted pathway enables CO_2 dissociation with a substantially lower energy barrier compared to direct dissociation. Furthermore, the catalytic cycle maintains sustainability through dynamic surface regeneration: The transient Mo-OH species formed during reaction undergoes rapid dehydrogenation in the H_2-rich environment (Fig. 3 and Supplementary Fig. S35), reconstructing the active Mo-O/Mo-N configuration that perpetuates the catalytic cycle. The superior catalytic performance and stability of the HEMN system arise from a synergistic combination of favorable thermodynamics, lowered kinetic barriers, and self-repairing surface architecture. Based on the structural model of the (112) facet, we further evaluated alternative reaction pathways, namely, the HCOO* and *COOH routes, to theoretically exclude competing mechanisms. The results show that the H_2-assisted pathway features a significantly lower activation barrier (2.22 eV for the *COOH route and 1.45 eV for the *HCOO route, as shown in Supplementary Fig. S42), in good agreement with our in-situ DRIFTS measurements (Supplementary Fig. S28).

https://doi.org/10.1038/s41467-026-68756-y

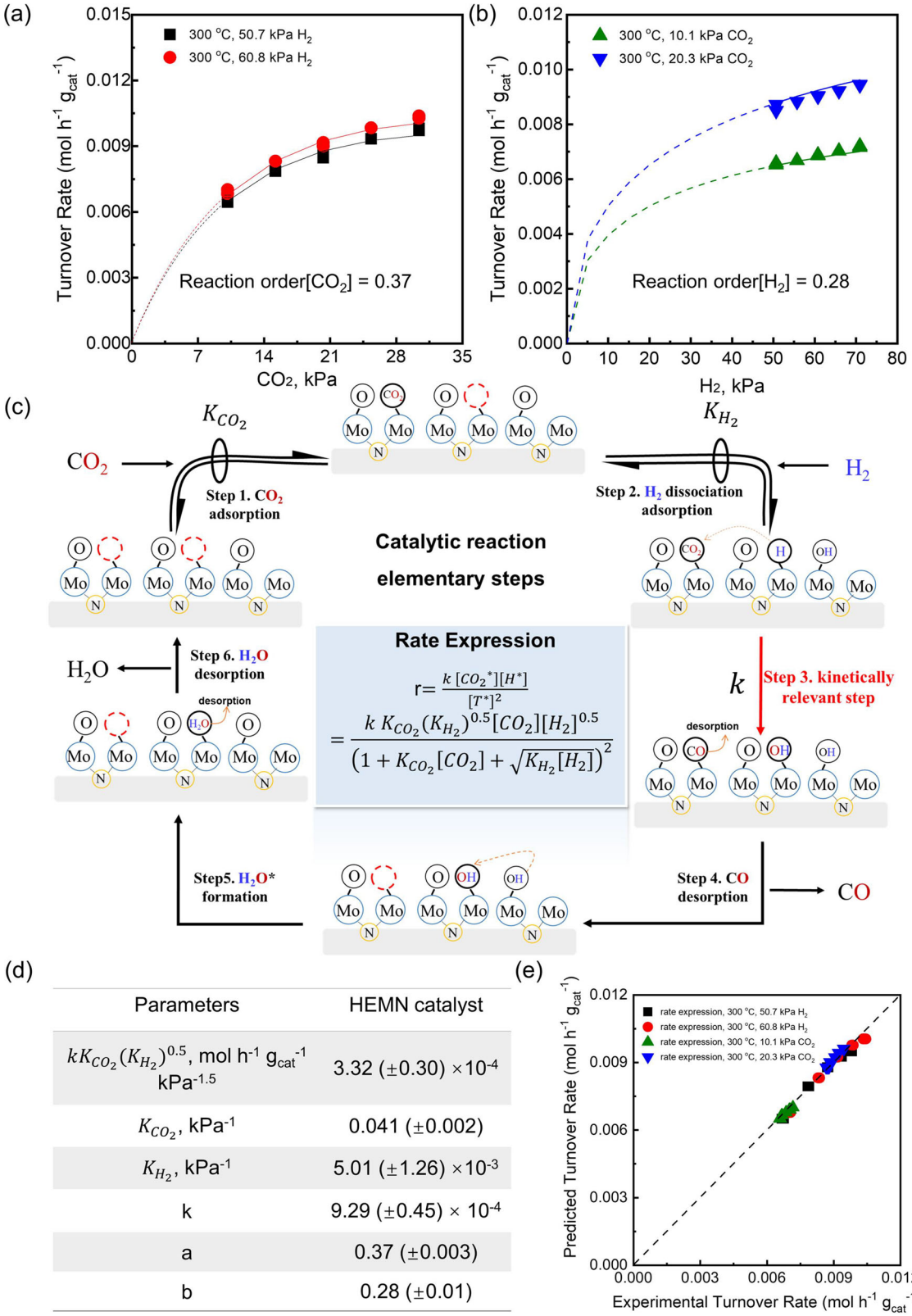

Parameters	HEMN catalyst
$kK_{CO_2}(K_{H_2})^{0.5}$, mol h^{-1} g_{cat}^{-1} $kPa^{-1.5}$	3.32 (±0.30) ×10^{-4}
K_{CO_2}, kPa^{-1}	0.041 (±0.002)
K_{H_2}, kPa^{-1}	5.01 (±1.26) ×10^{-3}
k	9.29 (±0.45) × 10^{-4}
a	0.37 (±0.003)
b	0.28 (±0.01)

Fig. 4 | Kinetic analysis of RWGSR over HEMN catalyst. a Effect of CO_2. **b** Effect of H_2. **c** Elementary steps on the HEMN catalyst. **d** Kinetic parameters derived from rate data regression. **e** Parity plot for the predicted and measured intrinsic rates on the HEMN catalyst. All turnover rates were corrected to 0.4–1.8 h time-on-stream. Kinetic testing conditions of the RWGSR over the HEMN catalyst reacted at 300 °C, ambient pressure with 50.7 kPa (■) or 60.8 kPa H_2 (●), and 10.1 kPa (▲) or 20.3 kPa CO_2 (▼), and a space velocity of 48,000 ml/g_{cat}/h.

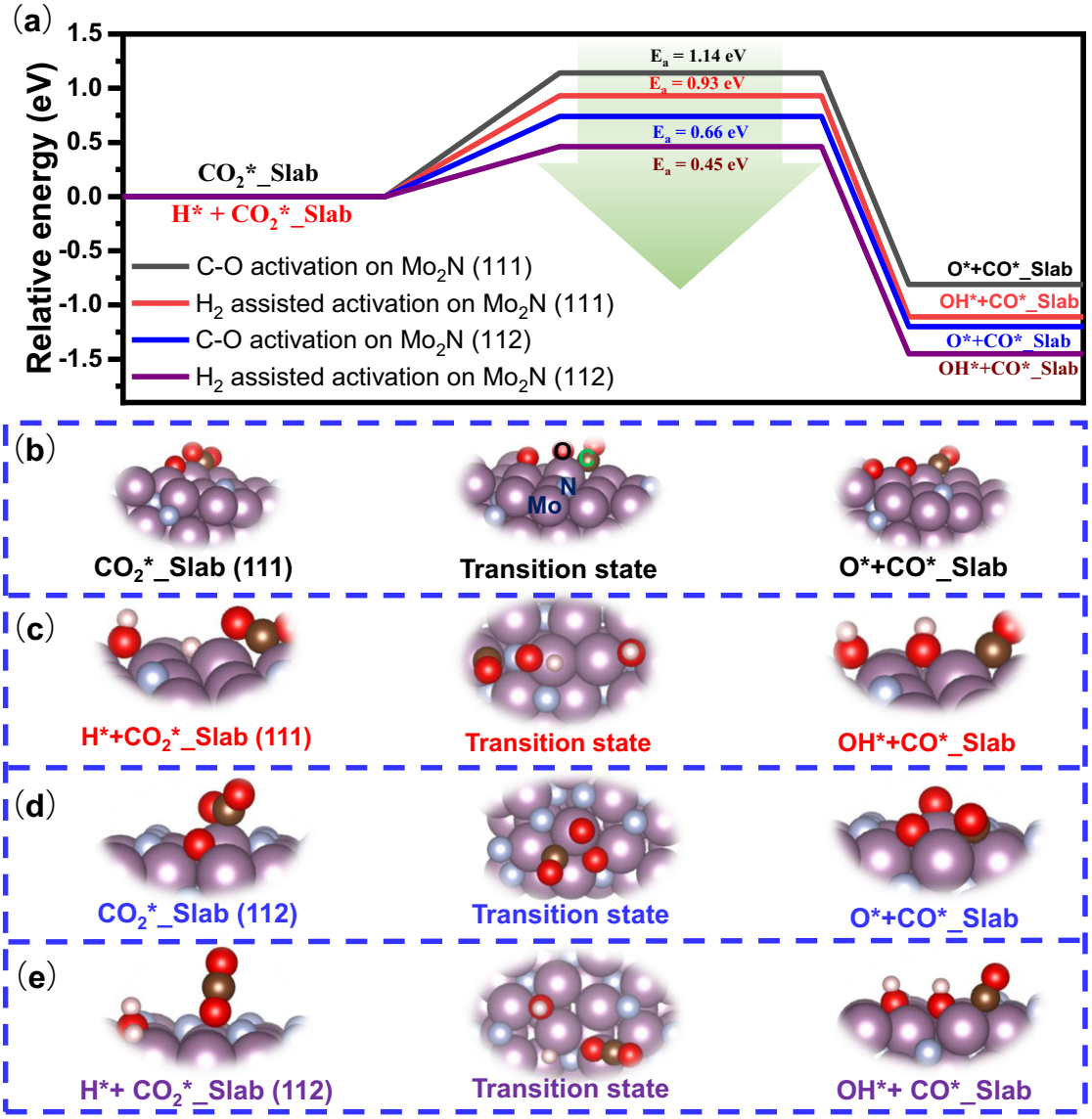

Fig. 5 | Energy barriers & structures for C–O activation on Mo_2N (111)/(112) with/without H*. a Reaction energy profiles for different pathways on the (111) and (112) facets. **b**–**e** Corresponding initial state, transition state, and final state structures.

Discussion

In summary, we report a novel synthesis strategy that integrates atmospheric modulation with self-driven ammonia decomposition to create a near-surface "quasi-hyperbaric" ammonia microenvironment, enabling in-situ formation of HEMN with dominant (112)-oriented facets. The resulting catalyst combines cost-effectiveness and synthetic simplicity with outstanding performance, achieving near-equilibrium CO_2 conversion (56%) and 100% CO selectivity at 550 °C with a space velocity at 24,000 ml/g_{cat}/h. It also demonstrates excellent stability, with ≤ 1% activity loss over 250 + hours of continuous operation and cycling. Remarkably, HEMN exceeds noble-metal behavior, maintaining 100% CO selectivity versus < 92% for a benchmark Pt-based catalyst at 550 °C. Mechanistic studies, including in-situ spectroscopy and DFT calculations, reveal that hybrid Mo-N/M-O motifs on (112) microfacets act as dual-functional active sites, enabling CO_2 activation via a hydrogen-assisted redox mechanism. This work not only deciphers crucial structure-activity relationships in transition metal nitrides but also establishes a robust design framework for developing non-precious, thermally robust catalysts with industrial-grade activity-selectivity – advancing the prospects of sustainable CO_2 valorization.

Methods

The synthesis of catalysts

The high-energy-micro-faceted molybdenum nitride (HEMN) catalysts. A precise amount of ammonium molybdate ($H_8MoN_2O_4$, Aladdin, AR grade) was dissolved in deionized water and uniformly dispersed onto silica or other supports using the incipient wetness impregnation method. The resulting slurry was dried at 100 °C for 12 h to obtain the precursor. Subsequent calcination was performed in a tubular furnace under flowing NH_3 at 600 °C (with a heating rate: 5 °C/min) for 4 h to yield the corresponding supported HEMN catalysts.

Synthesis of reference catalysts. (i) The pure Mo_2N catalyst was synthesized via a co-precipitation method. First, 3.5 g of ammonium molybdate ($H_8MoN_2O_4$, Aladdin, AR grade) and 3.6 g of melamine ($C_3H_6N_6$, Sigma, 99%) were separately dissolved in 50 mL deionized water. The solutions were combined under continuous magnetic stirring to induce complete precipitation. The resulting precipitate was isolated by centrifugation, dried at 120 °C for 12 h, and subjected to temperature-programmed calcination in a tubular furnace under N_2 flow. The thermal profile

included a ramp from ambient temperature to 800 °C at 10 °C/min for 7 h; (ii) The CeO_2 support was prepared by calcining 6 g of cerium nitrate ($Ce(NO_3)_3$, Macklin, AR grade) in a muffle furnace at 350 °C at 5 °C/min for 2 h. Separately, 14.88 mg of platinum tetra-ammine nitrate ($H_{12}N_6O_6Pt$, Aladdin, 99.9%) was dissolved in 525 µL deionized water and impregnated onto 1.5 g of the pre-synthesized CeO_2 support using the incipient wetness impregnation method. The impregnated material was dried at 80 °C for 12 h and activated in a muffle furnace under static air with a thermal ramp of 5 °C/min to 800 °C, where it was held for 1 h; (iii) The Ni/Al_2O_3 catalyst was prepared by dissolving 148.5 mg of nickel nitrate hexahydrate ($Ni(NO_3)_2{\cdot}6H_2O$, Macklin, AR grade) in 1150 µL deionized water. The solution was impregnated onto 1.5 g of γ-Al_2O_3 support via the incipient wetness method. The composite was dried at 100 °C for 12 h and calcined in a muffle furnace with a 5 °C/min ramp to 600 °C for 4 h. (iv) The CuZnAl catalyst was prepared by co-precipitation. An aqueous solution of Cu, Zn, and Al nitrates and a separate K_2CO_3 solution were simultaneously added dropwise into a beaker at 80 °C with vigorous stirring. The pH was maintained at approximately 9 during this process. The resulting suspension was aged at 80 °C for 12 h, then the precipitate was collected, washed with deionized water, dried at 100 °C for 12 h, and finally calcined at 550 °C for 4 h in air. (v) The Ni/CeO_2 catalyst was prepared by incipient wetness impregnation of the CeO_2 support with an aqueous solution of nickel nitrate. The material was subsequently dried at 100 °C for 12 h and calcined at 300 °C for 2 h (ramp rate: 5 °C/min). Prior to catalytic testing, the catalyst was reduced in a 5% H_2/Ar flow at 550 °C for 2 h. (vi) The Fe/ZrO_2 catalyst with an iron loading of 1.43 wt% was prepared by the incipient wetness impregnation of a ZrO_2 support with an aqueous solution of ferric nitrate. The precursor was dried at 100 °C for 12 h and subsequently calcined at 450 °C for 4 h in static air with a heating rate of 5 °C/min. Prior to catalytic testing, the catalyst was reduced at 550 °C for 2 h in a 5% H_2/Ar (30 mL/min). (vii) The Pt/SiO_2 catalyst was prepared by the incipient wetness impregnation of a SiO_2 support with an aqueous solution of tetra-ammine-platinum(II) nitrate. Following impregnation, the material was dried at 100 °C for 12 h and subsequently calcined at 450 °C for 2 h in static air with a heating rate of 10 °C/min. (viii) The $Ru/\gamma\text{-}Al_2O_3$ catalyst was prepared by the incipient wetness impregnation of a γ-Al_2O_3 support with an aqueous solution of ruthenium(III) chloride. The resulting material was dried at 100 °C for 12 h and subsequently calcined at 500 °C for 2 h in static air with a heating rate of 10 °C/min. Prior to catalytic testing, the catalyst was reduced in a 5% H_2/Ar flow (30 mL/min) at 550 °C for 1 h.

The performance of catalysts

After synthesizing the HEMN catalyst under an ammonia atmosphere, we evaluated its performance of RWGSR. The RWGSR tests were conducted in a home-made fixed-bed reactor system, which consists of a quartz tube with an inner diameter of 8 mm. The catalyst was prepared by pelletizing, crushing, and sieving to 60–80 mesh, followed by homogeneous mixing with quartz sand. The reaction was carried out at 1 atm with a feed gas mixture of CO_2, H_2, and N_2 in a volumetric ratio of 24:72:4. During the temperature-programmed process, the reaction gas mixture was continuously fed into the reactor. After reaching the target temperature, the system was stabilized for 30 minutes before data collection. Product analysis was performed using an online gas chromatograph (GC2060, Shanghai Ruimin Instrument Co., Ltd.) equipped with a flame ionization detector (FID; Rt-Q-BOND column) and a thermal conductivity detector (TCD; TDX-01 column). A high-temperature conversion furnace was integrated into the system, and all product lines were maintained at 150 °C to ensure accurate online detection. CO_2 conversion and product selectivity were calculated via the carbon normalization method, with specific formulas provided as (2) and (3).

$$Con(\%) = \frac{\left(\sum N_i \cdot A_i \cdot f_i\right)_{in} - \left(\sum N_i \cdot A_i \cdot f_i\right)_{out}}{\left(\sum N_i \cdot A_i \cdot f_i\right)_{in}} * 100 \quad (2)$$

$$Sel(\%) = \frac{N_{pi} \cdot A_{pi} \cdot f_{pi}}{\sum N_{pi} \cdot A_{pi} \cdot f_{pi}} * 100 \quad (3)$$

Here, i denotes any gaseous species in the reaction system; N represents the number of carbon atoms in the component; A_i *and* f_i correspond to the chromatographic peak area and calibration factor of species i, respectively; and p denotes the products.

Detailed kinetic testing parameters are provided in Supplementary Tables S3, S4, with corresponding conversion and product selectivity data available in Supplementary Tables S7–S14.

The characterization of catalysts

X-ray diffraction (XRD) measurements were conducted on a Rigaku SmartLab 9 kW Advanced powder X-ray diffractometer using Cu Kα radiation (λ = 0.154 nm). The 2θ scanning range was 10° to 80° at a rate of 5°/min. **X-ray photoelectron spectroscopy (XPS)** analysis was performed using a Thermo Scientific K-Alpha instrument. Binding energy results were calibrated by referencing the C1s peak to 284.6 eV. The **specific surface area** was determined using the Brunauer–Emmett–Teller (BET) equation by analyzing the adsorption branch of the isotherm in the pressure range of $P/P_0 = 0.04–0.32$. Pore size distribution was derived from the adsorption branch using the Barrett–Joyner–Halenda (BJH) method, and the total pore volume was measured at $P/P_0 = 0.99$. **Temperature-programmed reduction and desorption analyses (H_2-TPR, H_2-TPD, CO_2-TPD)** were conducted on a home-made system equipped with an online mass spectrometer (Tilon SRD200M). For all experiments, 100 mg of catalyst was pretreated in Ar at 300 °C for 2 h to eliminate surface impurities. In H_2-TPR, the sample was reduced with 5% H_2/Ar while heating from room temperature to 900 °C at 10 °C/min, monitoring H_2 (m/z = 2) and H_2O (m/z = 18). For H_2-TPD, after H_2 adsorption (5% H_2/Ar, 1 h) and Ar purging, H_2 desorption was tracked (m/z = 2) during heating to 800 °C at 10 °C/min. Similarly, CO_2-TPD involved CO_2 adsorption (30% CO_2/N_2, 1 h), Ar purging, and monitoring CO_2 (m/z = 44) during heating to 800 °C at 10 °C/min under Ar flow. **High-angle annular dark-field scanning transmission electron microscopy (HAADF-STEM)** and **integrated differential phase contrast imaging (iDPC-STEM)** were performed using a Thermo Scientific Spectra 300 double spherical aberration-corrected transmission electron microscope operated at 300 kV with a convergence semi-angle of 25 mrad. The sample was dispersed in anhydrous ethanol via ultrasonication, deposited onto a grid using a micropipette, dried, and loaded into the microscope. In-situ **diffuse reflectance infrared Fourier transform spectroscopy (DRIFTS)** experiments were conducted using a Thermo Scientific Nicolet iS50 spectrometer equipped with an MCT detector. For RWGSR studies, the HEMN catalyst was pretreated in N_2 at 300 °C for 1 h, cooled to room temperature, and background spectra were collected at 300–600 °C under N_2. Reaction gas ($CO_2/H_2/N_2 = 24/72/4$) was then introduced into the in-situ cell to monitor intermediates and products. To investigate surface hydroxyl species interacted with H_2, the pretreated catalyst was exposed to 5% H_2/Ar from 25 to 300 °C, with spectra recorded in the range of 4000–2500 cm^{-1}. In-situ **XRD** was performed using a PANalytical Empyrean diffractometer equipped with a Cu Kα radiation source (λ = 1.5418 Å) at 40 kV and 40 mA. In-situ experiments were operated with a diffractometer equipped with a high-temperature reaction cell (XRK 900, Anton Paar GmbH).

All XRD patterns were scanned from 10° to 80° (2θ) at a rate of 5° min^{-1}. Temperature-programmed in-situ XRD measurements of the HEMN catalyst were performed under a mixed gas atmosphere of CO_2:H_2:Ar = 72:24:4 (vol%) with a total flow rate of 40 mL min^{-1}. The catalyst was heated from 25 °C to 50 °C, 400 °C, 500 °C, 550 °C, and 600 °C sequentially at a ramp rate of 10 °C min^{-1}, with one diffraction pattern collected at each target temperature. Subsequently, the catalyst was held at 600 °C for 60 min, during which diffraction patterns were collected every 20 minutes (3 patterns in total). For the in-situ **HRTEM** characterization, the data were acquired using an FEI ETEM equipped with a GATAN K3 direct electron detection camera, combined with a DENS MEMS-based gas sample holder. First, a small amount of an aqueous solution of the HEMN catalyst was precisely drop-cast onto the silicon nitride membrane window of the gas chip and subsequently air-dried at room temperature. Finally, the gas chip loaded with the sample was carefully installed into the in-situ gas holder. At the beginning of the in-situ experiment, a mixed gas of CO_2 and H_2 was introduced, while the temperature was simultaneously and gradually increased to 600 °C and held stable for 1 h. During this process, dynamic HRTEM images of the sample were acquired along the [021] zone axis. **The TPSR experiment** was conducted using a custom-built system equipped with an online mass spectrometer (Tilon SRD200M). Prior to the reaction, 100 mg of the catalyst was pretreated in argon at 300 °C for 2 h to remove surface impurities. The sample was then exposed to a 30% CO_2/N_2 gas mixture (flow rate: 20 mL/min) while heating from room temperature to 600 °C at a rate of 10 °C/min. The desorption signals of CO_2 (m/z = 44) and CO (m/z = 28) were continuously monitored. The In situ **Raman spectra** with CO_2/Ar were recorded on a Renishaw in Via spectrometer with 532 nm laser excitation, coupled with a Linkam TS 1500 micro in-situ cell. The HEMN was exposed to a 10% CO_2/Ar flow (30 mL/min) during the heating process. A reference spectrum was first collected at room temperature. The sample was then heated at 10 °C/min to 300 °C to 600 °C and then kept for 60 min. At each target temperature, the sample was stabilized, repositioned under the microscope, and two consecutive Raman scans were collected (60 s integration, spectral range: 100–1200 cm^{-1}).

Derivation of rate expression

The rate expression is derived based on the sequence of elementary steps proposed in Fig. 4c in the manuscript, considering the interaction between CO_2* and H* as the kinetically relevant step (**Step 3**, main manuscript) and the pseudo steady-state approximation of all intermediates.

$$r = k\theta_{CO_2^*}\theta_{H^*} \tag{4}$$

where r and k represent the turnover rate and rate constant of **Step 3**, respectively. θ_i denotes the fractional coverage of surface species j (j = *, CO_2*, H*). According to the Langmuirian adsorption model, the overall site balance is

$$\theta_* + \theta_{CO_2^*} + \theta_{H^*} = 1 \tag{5}$$

The quasi-equilibrium assumption on CO_2 adsorption (**Step 1**) and H_2 dissociative adsorption (**Step 2**) gives

$$\theta_{CO_2^*} = K_{CO_2}[CO_2]\theta_* \tag{6}$$

$$\theta_{H^*} = \sqrt{K_{H_2}[H_2]}\theta_* \tag{7}$$

where K_i (i = CO_2 or H_2) is the equilibrium constant of CO_2 adsorption or H_2 dissociative adsorption.

Substituting Eqs. 6–7 into Eq. 5 gives

$$\theta_* + K_{CO_2}[CO_2]\theta_* + \sqrt{K_{H_2}[H_2]}\theta_* = 1 \tag{8}$$

Thus,

$$\theta_* = \frac{1}{1 + K_{CO_2}[CO_2] + \sqrt{K_{H_2}[H_2]}} \tag{9}$$

Substituting **(6), (7), and (9)** into **(4)** gives **(1)** in the main manuscript.

Density functional theory (DFT)

Density functional theory (DFT) calculations were conducted using the Vienna ab initio simulation package (VASP 5.4.4)[34]. The exchange-correlation energy was modeled with the Perdew-Burke-Ernzerhof (PBE) functional under the generalized gradient approximation (GGA)[35]. Core electrons were described using projected-augmented wave (PAW) pseudopotentials, and a plane-wave cutoff energy of 450 eV was employed[36]. After conducting k-point convergence tests (as shown in Table S5), we ultimately determined that a Γ-centered 2 × 1 × 1 k-point grid was employed for the (111) facet, and a 2 × 2 × 1 grid was used for the (112) facet in the k-point sampling process. Convergence criteria were set to 10^{-5} eV for electronic relaxation and -0.05 eV/Å for ionic relaxation. Based on electron microscopy analysis, the synthesized Mo_2N material predominantly exposes the high-surface-energy (112) facet (Fig. 1 in the main manuscript). To explore its surface properties, we constructed a computational model of the Mo_2N (112) facet with lattice parameters of a = 12.0366 Å, b = 9.9712 Å, c = 21.0606 Å and angles of α = 90.0 °, β = 90.0 °, γ = 90 °. For comparative purposes, a thermodynamically stable Mo_2N (111) supercell model was also established (Supplementary Figs. S39, 40), with lattice parameters of a = 12.0366 Å, b = 18.0350 Å, c = 19.9984 Å, and angles of α = 90.0 °, β = 90.0 °, γ = 109.5 °. In the computational setup, the bottom atomic layers were fixed to simulate the bulk catalyst's structural rigidity, while the top surface layers were fully relaxed to capture local atomic rearrangements during adsorption and surface reactions. This approach strikes a balance between computational efficiency and accuracy, ensuring the identification of the most stable configurations during adsorption-reaction processes. The climbing image nudged-elastic-band method (CI-NEB), including six replicas, was used to search the transition states (TS) for all of the elementary reactions. The TS was denoted by the highest image along the minimum energy path. The energy barrier (E_a) of each elementary reaction was calculated by the energy difference between the TS and the initial state (IS) without inclusion of the zero-point energy. Vibrational frequencies were computed at the optimized transition state structure using the finite-displacement method to determine the Hessian (force constant) matrix (Supplementary Table S6). The calculation was performed with IBRION = 5, a displacement step of POTIM = 0.015 Å, and the same exchange-correlation functional and pseudopotentials as used in the transition state optimization. NSW was set to 1 to prevent any further geometry relaxation. The vibrational mode corresponding to the imaginary frequency was visualized using "Jmol" (an open-source Java viewer), confirming that the atomic displacements align with the expected reaction coordinate.

The adsorption energy (E_{ads}) of adsorbates on all slab models was calculated as below:

$$E_{ads} = E_{total} - (E_{slab} + E_g) \tag{10}$$

where E_{total}, E_{slab}, and E_g represent the total energy of the adsorbed system, the pristine slab energy, and the gas-phase adsorbate energy, respectively. Correspondingly, the desorption energy (E_{des}) is defined

as below:

$$E_{des} = (E_{slab} + E_g) - E_{total} \quad (11)$$

The vacancy formation energy (ΔE_f) of HEMN catalysts was calculated as below:

$$\Delta E_f = E_{slab} - (E_v + E_{H2O(g)}) \quad (12)$$

where, E_v denotes the energy of the vacancy-containing surface, and $E_{H2O(g)}$ represents the energy of an isolated water molecule in the gas phase.

The surface energy calculation involves three key steps: First, both the bulk material and the surface models (as illustrated in Supplementary Fig. S1) undergo geometric optimization to ensure they correspond to their lowest-energy stable configurations. Second, the bulk energy E_{bulk} is calculated, and the average energy per atom $E_{bulk,\,per\,atom}$ is determined using the formula ($E_{bulk,peratom} = E_{bulk}/N_{bulk}$, where N_{bulk} is the number of atoms in the bulk material). Third, the total energy of the surface model E_{slab} is computed. The surface energy $\gamma_{surface}$ is then calculated using the following formula:

$$\gamma_{surface} = \frac{1}{2A}(E_{slab} - N_{slab} \times E_{bulk,peratom}) \quad (13)$$

where: A is the surface area, N_{slab} is the number of atoms in the surface model. For the surface model with adsorbed ammonia, which simulates the surface energy under an ammonia atmosphere, the calculation formula is as follows:

$$\gamma_{surface,NH_3} = \frac{1}{2A}(E_{slab,NH_3} - N_{slab} \times E_{bulk,peratom} - N_{NH_3} \times E_{NH_3}) \quad (14)$$

where E_{slab,NH_3} represents the total energy of the surface model with adsorbed ammonia, N_{NH_3} is the number of ammonia molecules adsorbed on the surface, and E_{NH_3} is the energy of a single ammonia molecule in the gas phase.

Data availability

All data generated in this study are provided in the Supplementary Information/Source Data. All data are available from the corresponding author upon request.

References

1. Xin, H. et al. Reverse water gas-shift reaction product driven dynamic activation of molybdenum nitride catalyst surface. *Nat. Commun.* **15**, 3100 (2024).
2. Wang, H. et al. Synergistic interactions of neighboring platinum and iron atoms enhance reverse water–gas shift reaction performance. *J. Am. Chem. Soc.* **145**, 2264–2270 (2023).
3. Liu, H. et al. Partially sintered copper-ceria as excellent catalyst for the high-temperature reverse water gas shift reaction. *Nat. Commun.* **13**, 867 (2022).
4. Bahmanpour, A. M. et al. Recent progress in syngas production via catalytic CO_2 hydrogenation reaction. *Appl. Catal. B Environ.* **295**, 120319 (2021).
5. Ahmadi, K. M. et al. An active, stable cubic molybdenum carbide catalyst for the high-temperature reverse water-gas shift reaction. *Science* **384**, 540–546 (2024).
6. Guo, J. et al. In–Ni intermetallic compounds derived from layered double hydroxides as efficient catalysts toward the reverse water gas shift reaction. *ACS Catal.* **12**, 4026–4036 (2022).
7. Wang, R. et al. High-energy facet engineering for electrocatalytic applications. *Small* **20**, 2401546 (2024).
8. Zhang, R. et al. Synergism of ultrasmall Pt clusters and basic $La_2O_2CO_3$ supports boosts the reverse water gas reaction efficiency. *Adv. Energy Mater.* **13**, 2203806 (2023).
9. Zhao, Z. et al. Atomically dispersed Pt/CeO_2 catalyst with superior CO selectivity in reverse water gas shift reaction. *Appl. Catal. B Environ.* **291**, 120101 (2021).
10. Yang, X. et al. Promotion effects of potassium on the activity and selectivity of Pt/zeolite catalysts for reverse water gas shift reaction. *Appl. Catal. B Environ.* **216**, 95–105 (2017).
11. Zakharova, A. et al. Reverse microemulsion-synthesized high-surface-area $Cu/\gamma\text{-}Al_2O_3$ catalyst for CO_2 conversion via reverse water gas shift. *ACS Appl. Mater. Interfaces* **14**, 22082–22094 (2022).
12. Gu, M. et al. Structure-activity relationships of copper-and potassium-modified iron oxide catalysts during reverse water-gas shift reaction. *ACS Catal.* **11**, 12609–12619 (2021).
13. Lin, Z. et al. Transition metal carbides and nitrides as catalysts for thermochemical reactions. *J. Catal.* **404**, 929–942 (2021).
14. Tian, D. et al. Density functional theory studies of transition metal carbides and nitrides as electrocatalysts. *Chem. Soc. Rev.* **50**, 12338–12376 (2021).
15. Wang, H. et al. Transition metal nitrides for electrochemical energy applications. *Chem. Soc. Rev.* **50**, 1354–1390 (2021).
16. Zhou, H. et al. Two-dimensional molybdenum carbide 2D-Mo_2C as a superior catalyst for CO_2 hydrogenation. *Nat. Commun.* **12**, 5510 (2021).
17. Jurado, A. et al. Molecular mechanism and microkinetic analysis of the reverse water gas shift reaction heterogeneously catalyzed by the Mo_2C MXene. *ACS Catal.* **12**, 15658–15667 (2022).
18. Wu, Y. et al. The highly selective catalytic hydrogenation of CO_2 to CO over transition metal nitrides. *Chin. J. Chem. Eng.* **43**, 248–254 (2022).
19. Gao, Z. et al. Shielding $Pt/\gamma\text{-}Mo_2N$ by inert nano-overlays enables stable H_2 production. *Nature* **638**, 690–696 (2025).
20. Nagae, M. et al. Microstructure of a molybdenum nitride layer formed by nitriding molybdenum metal. *J. Am. Ceram. Soc.* **84**, 1175–1177 (2001).
21. Zhang, X. et al. Highly dispersed copper over $\beta\text{-}Mo_2C$ as an efficient and stable catalyst for the reverse water gas shift (RWGS) reaction. *ACS Catal.* **7**, 912–918 (2016).
22. Hameed, G. et al. Experimental optimization of Ni/P atomic ratio for nickel phosphide catalysts in reverse water-gas shift. *J. CO_2 Util.* **77**, 102606 (2023).
23. Gao, P. et al. Novel heterogeneous catalysts for CO_2 hydrogenation to liquid fuels. *ACS Cent. Sci.* **6**, 1657–1670 (2020).
24. Wang, Q. et al. One-dimensional MoO_3 coated by carbon for supercapacitor with enhanced electrochemical performance. *J. Mater. Sci. Mater El.* **30**, 6643–6649 (2019).
25. Yu, Z. et al. Formic acid as a bio-CO carrier: selective dehydration with $\gamma\text{-}Mo_2N$ catalysts at low temperatures. *ACS Sustain. Chem. Eng.* **8**, 13956–13963 (2020).
26. Liu, H. et al. Direct cleavage of C=O double bond in CO_2 by the subnano MoO(x) surface on Mo_2N. *Nat. Commun.* **15**, 9126 (2024).
27. Ye, R. et al. CO_2 hydrogenation to high-value products via heterogeneous catalysis. *Nat. Commun.* **10**, 5698 (2019).
28. Jin, F. et al. Unraveling the influence of oxygen vacancies in MoO_x catalysts on CO_2 hydrogenation. *Chem. Eng. J.* **495**, 153333 (2024).
29. Wang, Y. et al. Breaking the linear scaling relationship of the reverse water–gas–shift reaction via construction of dual-atom Pt–Ni pairs. *ACS Catal.* **13**, 3735–3742 (2023).
30. Sun, X. et al. Reaction-induced unsaturated Mo oxycarbides afford highly active CO_2 conversion catalysts. *Nat. Chem.* **16**, 2044–2053 (2024).
31. Gong, Y. et al. In Situ Surface Restructuring of $\gamma\text{-}Mo_2N$ for Enhanced Reverse Water-GasShift Reaction. *ACS Catal.* **15**, 8337–8344 (2025).

32. Santiago, C. M. et al. FT-IR examination of the development of secondary cell wall in cotton fibers. *Fibers* **3**, 30–40 (2015).
33. Langer, M. et al. Kinetic modeling of dynamically operated heterogeneously catalyzed reactions: Microkinetic model reduction and semi-mechanistic approach on the example of the CO_2 methanation. *Chem. Eng. J.* **467**, 143217 (2023).
34. Kresse, G. et al. Efficient iterative schemes for Ab initio total-energy calculations using a plane-wave basis set. *Phys. Rev. B.* **54**, 11169 (1996).
35. Perdew, J. P. et al. Generalized gradient approximation made simple. *Phys. Rev. Lett.* **77**, 3865–3868 (1996).
36. Kresse, G. et al. From ultrasoft pseudopotentials to the projector augmented-wave method. *Phys. Rev. B.* **59**, 1758–1775 (1999).

Acknowledgements

This work was supported in part by the National Key Research and Development Program of China (2022YFE0113800), the National Natural Science Foundation of China (No. 22279115, 22122505, 22075250, 22208299), the Natural Science Foundation of Zhejiang Province (No. LBMHZ25B030005) and the Zhejiang Province Leading Earth Goose Program (2025c02224). The authors acknowledge Prof. Jianguo Wang' Group for providing computational resources and technical support.

Author contributions

J.T., H.C., X.L., Y.W., and Y.Z. conceived and designed the project. L.F., L.X., and Z.W. carried out the catalytic reactions and performed initial characterizations. L.F. conducted the X-ray related analyses (XRD, and XPS), DRIFTS studies, and temperature-programmed experiments. H.C. performed and analyzed the kinetic experiments. Q.F., L.X., and X.J. carried out electron microscopy measurements and analysis. N.O. and J.T. performed the DFT calculations. J.T. wrote the original manuscript. J.T., L.F., N.O., L.X., Z.W., H.C., Q.F., X.J., J.Z., M.T., L.Z., Y.W., X.L., and Y.Z. participated in discussing the results and revising the paper.

Competing interests

The authors declare no competing interests.

Additional information

Supplementary information The online version contains supplementary material available at https://doi.org/10.1038/s41467-026-68756-y.

Correspondence and requests for materials should be addressed to Haiting Cai, Yong Wang, Xiaonian Li or Yihan Zhu.

Peer review information *Nature Communications* thanks the anonymous reviewers for their contribution to the peer review of this work. A peer review file is available.